**Invited paper**

Chenjie Zeng*

# Precision at the nanoscale: on the structure and property evolution of gold nanoclusters

https://doi.org/10.1515/pac-2018-0511

**Abstract:** Chemists are often regarded as "architects", who are capable of building up complex molecular structures in the ultrasmall-dimensional world. However, compared with organic chemistry, nanochemistry – which deals with nanoparticles in the size range from 1 to 100 nm – is less precise in terms of synthesis, composition, and structure. Such an imprecise nature of nanochemistry has impeded an in-depth understanding as well as rational control of structures and properties of nanomaterials. Motivated by this, thiolate-protected gold nanoclusters (denoted as $Au_n(SR)_m$) have recently emerged as a paradigm of atomically precise nanomaterials, in which all the nanoparticles are identical to each other with the same number of core atoms ($n$) and surface ligands ($m$) as well as the atomic arrangement. In this review, we provide a demonstration of how the precise nature of $Au_n(SR)_m$ nanoclusters allows one to understand, decipher and discover some important, enigmatic and intriguing issues and phenomena in nanoscience, including (i) a precise nanoscale transformation reaction induced by surface ligand exchange, (ii) the total structures of crystalline metal phases and the self-assembled surface monolayers, (iii) the periodicities and quantum confinement in nanoclusters and (iv) the emergence of hierarchical complexity in the entire nanoparticle system. We expect that such an in-depth understanding will eventually lead to the rational design and precise engineering of complex architectures at the nanoscale.

**Keywords:** complexity; emergence; gold nanoclusters; hierarchy; IUPAC-SOLVAY International Award for Young Chemists; ligand exchange; magic size; nanochemistry; periodicity; phase and surface; precision; self-assembly.

## Introduction

The past three decades have seen significant advancements in nanoscience and nanotechnology. Despite such fast development, some fundamental issues associated with nanomaterials still challenge nanochemists and remain to be solved. For example, it is difficult to achieve a comprehensive understanding of the chemistry for nanocrystal synthesis, since nanocrystal is an complex object assembled from tens to millions of atoms and molecules, and its synthesis involves intertwined reactions which are further affected by the kinetics of nucleation, growth, and shape-control. Often, nanomaterial synthesis is largely based on the empirical trial and error rather than rational design and control. Also, the surface structures, which are crucial to the stability, solubility, charge transport, catalytic activity, etc., remain elusive due to the difficulties in the two-dimensional characterization. Last but not least, nanoparticles are not identical to each other: even the nanoparticles with the highest monodispersity may contain a different number of atoms for each

**Article note:** A collection of peer-reviewed articles by the winners of the 2017 IUPAC-SOLVAY International Award for Young Chemists.

***Corresponding author: Chenjie Zeng,** Department of Chemistry, University of Pennsylvania, Philadelphia, PA, 19104, USA; and Department of Chemistry, Carnegie Mellon University, Pittsburgh, PA, 15213, USA, e-mail: chenjiez@sas.upenn.edu, zengchenjie0@gmail.com. http://orcid.org/0000-0002-2904-5590

nanoparticle, not to mention possibly different structures and impurities, which could preclude a precise correlation between the structure and properties.

One approach to solving these challenges is to improve characterizations. For example, state-of-art transmission electron microscopy techniques such as aberration-corrected TEM [1, 2], high-angle annular dark field (HADDF)-TEM [3, 4], single particle cryo-electron microscopy [5] etc., have been applied to map out the three-dimensional structures of nanoparticles with near atomic-resolution. Also, the nucleation, growth, transformation and assembly processes of nanoparticles are now being characterized by in situ liquid cell TEM as well as in situ grazing-incidence X-ray scattering [6–8].

Besides the efforts of improving the resolution of instruments, another approach to tackling the challenges is to increase the quality of nanoparticles: from the nanometer monodispersity to the atomic precision (Scheme 1). Commonly, the quality of nanoparticles is evaluated by TEM (Scheme 1a); but even the most monodisperse nanoparticles may have still a size deviation of ca. 5 % (Scheme 1b). Atomically precise nanoparticles are exactly identical to each other in composition and structure (Scheme 1c). Instead of measuring the nanometer sizes, the quality of atomically precise nanoparticles can be characterized by mass spectrometry (Scheme 1d), by which a single peak should be observed for atomically precise nanoparticles and accordingly the molar mass of the nanoparticles can be determined. In addition, if the single-crystals of atomically precise nanoparticles can be achieved, the total structures of nanoparticles (including the core, surface, and assembly) can be unambiguously characterized by X-ray crystallography (Scheme 1c), which is similar to the way that structures of giant biomolecules (e.g. DNA and proteins) are determined.

To achieve atomic precision in nanomaterials, akin to organic chemists synthesizing precise organic molecules, has long been a dream of nanochemists. This dream has recently been realized in thiolate-protected gold nanoclusters (denoted as $Au_n(SR)_m$) [10]. Nanoclusters are the ultrasmall nanoparticles in the size range from ~1 to ~3 nm and contain tens to thousands of core atoms. It took nearly two decades for the $Au_n(SR)_m$ nanoclusters

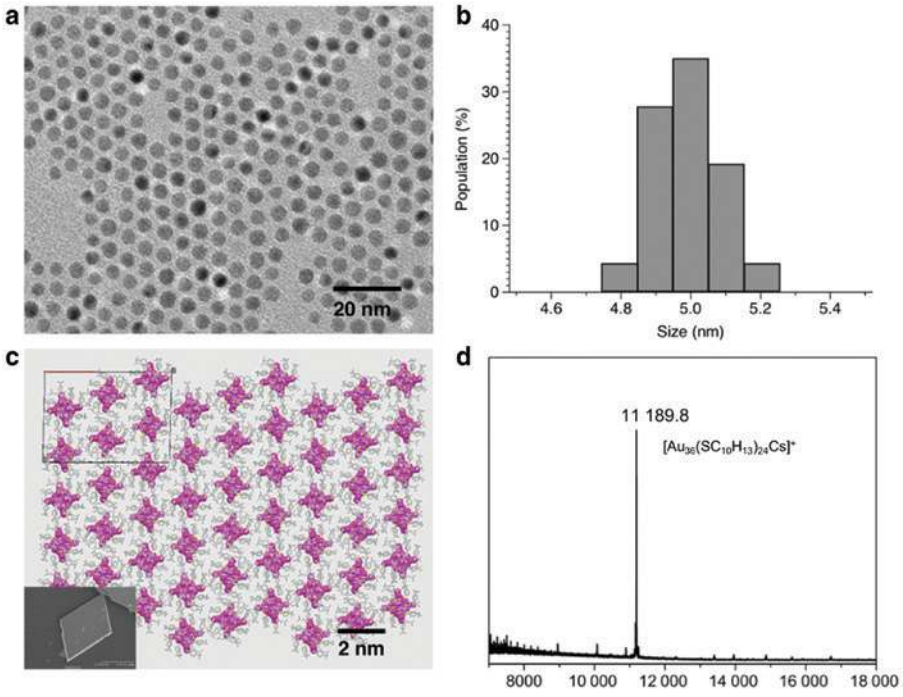


**Scheme 1:** Monodisperse nanoparticles vs atomically precise nanoclusters. (a) Monodisperse gold nanoparticles imaged by TEM. (b) Corresponding histogram of size distribution of gold nanoparticles ($5 \pm 0.3$ nm). (c) Atomically precise $Au_{36}(SC_{10}H_{13})_{24}$ nanoclusters revealed by X-ray crystallography; the inset picture is the corresponding single crystal imaged by scanning electron microscopy. (d) Electro-spray ionization mass spectrometry (ESI-MS) of the $Au_{36}(SC_{10}H_{13})_{24}$ nanoclusters. The single peak corresponds to the mass of the nanoclusters (Cs ion is added to facilitate ionization). Adapted with permission from Ref. [9].

to evolve from polydisperse to monodisperse and finally to atomic precise [11]. In the 1980s, Nuzzo, Whitesides, and coworkers discovered that the thiol molecules can spontaneously adsorb onto the crystalline surface of gold (or other metals) to form stable self-assembled monolayers (SAMs) [12, 13]. The benign chemistry between the gold and thiols was then exploited by Brust, Schiffrin, and coworkers to synthesize ultrasmall thiolate-protected gold nanoparticles with sizes distributed from 1 to 3 nm [14, 15]. In later 1990s, Whetten, Murray, and others carried out extensive work to increase the monodispersity of thiolate-protected gold nanoparticles, such as selective-size precipitation, chromatographic separation, etching and thermal treatment [16–21]. Tsukuda and Negishi further separated a series of "magic sizes" of water soluble gold nanoclusters containing 10–40 gold atoms in 2004 [22, 23]. Up to this point, the major efforts were focused on the separation of a mixture of nanoclusters and the yield of each size was low, which precluded in-depth studies and further applications of gold nanoclusters. The crystallization of $Au_n(SR)_m$ nanoclusters was not possible then.

Jin et al. subsequently tackled the synthesis by aiming at "one pot for one size" and high-yield synthesis of high purity $Au_n(SR)_m$ nanoclusters without the necessity of sophisticated size separation steps. A systematic "size focusing" method was established for preparing atomically precise gold nanoclusters [24]. The "size-focusing" consists of two-step. In the first step, polydispersed $Au_n(SR)_m$ nanoclusters but with a suitable size range are synthesized by reducing gold(I)-thiolate complexes in a controlled environment. In the second step, the mixture of gold nanoclusters is focused or transformed into a single size through applying harsh conditions (such as heating and etching by excess thiol). Since the stability of different sized nanoclusters varies significantly, only the most robust species survives the harsh size focusing process. The basic principle of the size focusing method is essentially "survival of the most robust", which is reminiscent of the "survival of the fittest" in nature's selection law. By the year of 2010, $Au_{25}(SC_2H_4Ph)_{18}$, $Au_{38}(SC_2H_4Ph)_{24}$ and $Au_{144}(SC_2H_4Ph)_{60}$ nanoclusters had been successfully synthesized in relatively large quantities and more importantly, with molecular purity [25–29]. The accessibility of these atomically precise nanoclusters significantly facilitated the studies of their structures and properties, and provided the foundation for further discovery in $Au_n(SR)_m$ nanocluster research.

In this review, we focus on the demonstration of the great promise of nanoscale precision in understanding, deciphering, and discovering some of the important, enigmatic and intriguing issues in nanoscience (Scheme 2). The promise of nanoscale precision is mainly demonstrated in the following five aspects: (i) the discovery of a precise nanoscale reaction, i.e. the "ligand-exchange induced size/structure transformation" (LEIST for short); (ii) the identification of diverse phases of gold nanoclusters and their relative stability;

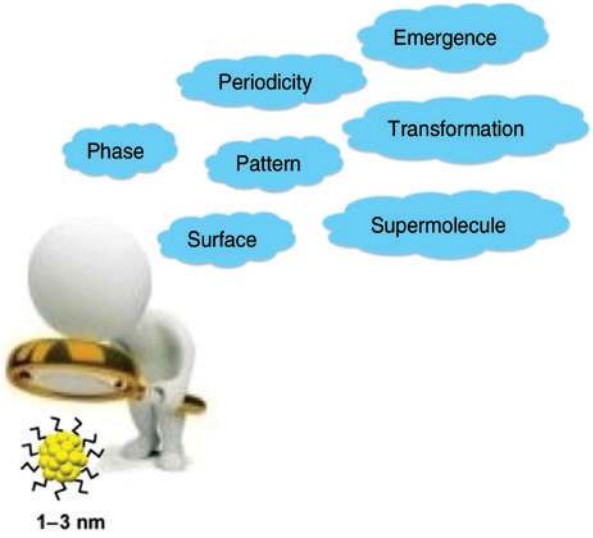


**Scheme 2:** The accessibility of the atomically precise nanoclusters and their crystal structures opens up opportunities to understand some fundamental and important issues in nanoscience.

(iii) the comprehensive understanding of the surface structures of nanoparticles from the binding motifs to the patterning symmetry in different environments; (iv) the discovery of periodicity in the size, structure and property of magic size nanoclusters; and (v) the emergence of hierarchical structural complexities in nanoparticles and their assemblies.

## Transformation: a precise nanoscale reaction

Reaction and transformation is an essential part of chemistry. Unlike conventional organic or inorganic chemistry, in which one molecule or compound can be precisely transformed to another during the chemical reaction, the chemistry at the nanoscale (such as the nucleation, growth, and shape control of nanocrystals) are unfortunately less precise and more difficult to understand and control. This is partly due to the still short history of nanochemistry (roughly three decades) compared with nearly two centuries for organic chemistry and even longer for inorganic chemistry. More importantly, nanoparticles, assembled from a large number of atoms (in the core) and molecules (in the protecting layer), are significantly more complex than their atomic or molecular building blocks. Nanochemistry not only deals with chemical bonds and strong atomic interactions at the atomic or molecular scale, but also involves the assembly of multiple components at the nanoscale via weaker intermolecular van der Waals, Coulomb interactions, etc. Due to such a complex nature, de novo synthesis of nanocrystals is heavily based on empirical "trial and error" rather than rational design and control. It is expected that if precise reaction pathways can be developed in nanoscale reactions, more elaborate and functionalized nanoscale architectures could be created. This apparently still requires tremendous efforts in nanochemistry.

The accessibility of atomically precise $Au_n(SR)_m$ nanoclusters opens up opportunities to study the precise transformation at the nanoscale. In 2012, Zeng et al. discovered that $Au_n(SR)_m$ nanoclusters can be transformed from one stable size to another during a simple ligand exchange process [30, 31]. This was first demonstrated in the transformation of $Au_{38}(SC_2H_4Ph)_{24}$ to $Au_{36}(TBBT)_{24}$ via reacting with an excess of 4-*tert*-butylbenzenethiol (TBBT) at 80 °C for several hours (Scheme 3b) [31]. Although there is only a two-gold-atom

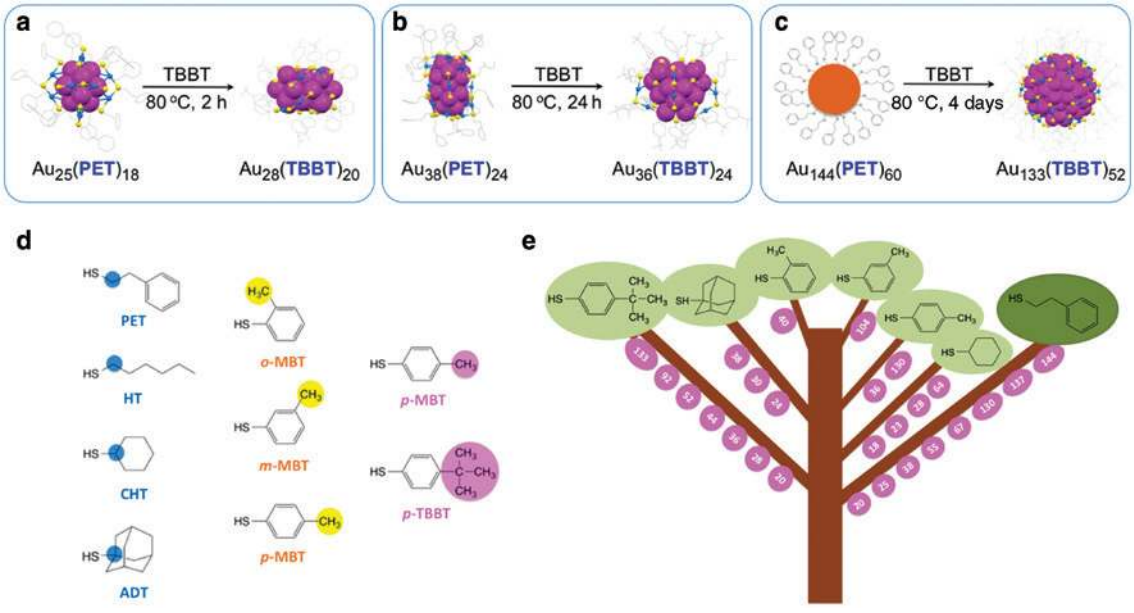


**Scheme 3:** Transformation of gold nanoclusters and the ligand effects. (a) Transformation from $Au_{25}(PET)_{18}$ to $Au_{28}(TBBT)_{20}$. (b) Transformation from $Au_{38}(PET)_{24}$ to $Au_{36}(TBBT)_{24}$. (c)Transformation from $Au_{144}(PET)_{60}$ to $Au_{133}(TBBT)_{52}$. (d) Three levels of ligand effects. (e) Expansion of the size library of $Au_n(SR)_m$ nanoclusters via tuning of the surface ligands. The numbers in pink spheres are the number of gold atoms (*n*).

difference between the sizes of the reactant and the product, the structure of nanoclusters is surprisingly transformed completely, i.e. from a 20-fold twinned (bi-)icosahedron to a single-crystalline truncated tetrahedron. The drastic transformation in the structure was unexpected, since ligand exchange was a common process to only adjust the surface properties of nanocrystals, and the core structure was considered to be preserved during ligand exchange. Such a "ligand-exchange induced size/structure transformation" (LEIST) process came as a surprise, and indeed was not an isolated case, as further work demonstrated the transformation from $Au_{25}(PET)_{18}$ to $Au_{28}(TBBT)_{20}$ (Scheme 3a) [32], and from $Au_{144}(PET)_{60}$ to $Au_{133}(TBBT)_{52}$ (Scheme 3c) [33]. As the size of nanocluster increases, a longer reaction time is usually required for the complete structural transformation (Scheme 3a–c).

The importance of LEIST process is manifold. (i) Akin to the transformation at the molecular scale (i.e. organic reactions), the LEIST reaction is a precise nanoscale reaction, which not only enables the synthesis of new nanoclusters with high yield (90 %) and high reproducibility, but also permits a detailed study of reaction mechanism (Fig. 1, vide infra). (ii) The LEIST reaction provides a fast route to the expansion of the "size library" of $Au_n(SR)_m$ nanoclusters compared with the de novo synthesis. (iii) The LEIST reaction demonstrates the significant contribution of surface ligands in the total energy minimization of the nanoclusters, and the size and structure of nanoclusters are highly sensitive to the subtle change of the surface ligands. By changing to different types of surface protecting thiolates (Scheme 3d), a large library of nanoclusters has been synthesized by both size focusing and size transformation methods (Scheme 3e). We note that such ligand effects are not simply the steric effect near the sulfur (i.e. α carbon), but are the conformation of the entire thiolate (Scheme 3d). For example, by simply adjusting the position of methyl group from *para*- to *meta*- to *ortho*-, the most stable size changes from $Au_{130}$ to $Au_{104}$ to $Au_{40}$, respectively [34]. The ligand effect can be further extended to the para-position of benzenethiol, which is farther away from the Au-S interface. It is found that, when the para group is methyl (MBT) or tertbutyl (TBBT), $Au_{130}$ and $Au_{133}$ are selected, respectively [35].

The simple and precise nature of the LEIST reaction permits the in-depth study of the transformation mechanism, as demonstrated in the transformation from $Au_{38}(SC_2H_4Ph)_{24}$ to $Au_{36}(TBBT)_{24}$ [36]. Aliquots of sample were extracted out from the reaction mixture at the different times and characterized by ESI–MS and UV-vis (Fig. 1). ESI–MS reveals the compositions (formula weights) of different types of intermediate nanoclusters, including the ligand-exchanged $Au_{38}(TBBT)_m(PET)_{24-m}$, sized-transformed $Au_{36}(TBBT)_m(PET)_{24-m}$ and $Au_{40}(TBBT)_{m+2}(PET)_{24-m}$ (Fig. 1a). On the other hand, UV-vis sheds light on the structures of these intermediate nanoclusters, based on their characteristic absorption peaks (Fig. 1b). Combining the results from ESI-MS and UV-vis, the transformation pathway from $Au_{38}(PET)_{24}$ to $Au_{36}(TBBT)_{24}$ can be mapped out, which includes following four stages (Fig. 1c).

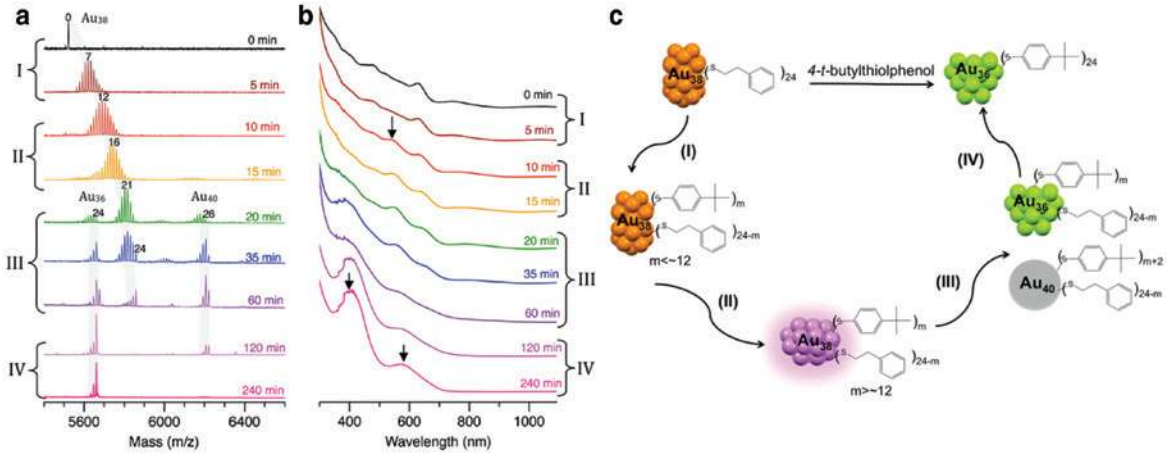


**Fig. 1:** The mechanism for the transformation from $Au_{38}(PET)_{24}$ to $Au_{36}(TBBT)_{24}$. (a) ESI–MS of the reaction intermediates. (b) Corresponding UV-vis. (c) Scheme of the transformation pathway. Adapted with permission from Ref. [36].

(I) Ligand exchange: $Au_{38}(PET)_{24} + TBBT \rightarrow Au_{38}(TBBT)_m(PET)_{24-m} + PET$ ($m <$ ca.12)
(II) Structure distortion: $Au_{38}(TBBT)_m(PET)_{24-m\ (m<ca.12)} + TBBT \rightarrow Au_{38}{}^*(TBBT)_m(PET)_{24-m\ (m>ca.12)} + PET$
(III) Disproportionation: $2Au_{38}{}^*(TBBT)_m(PET)_{24-m} + 2TBBT \rightarrow Au_{36}(TBBT)_m(PET)_{24-m} + Au_{40}(TBBT)_{m+2}(PET)_{24-m}$
(IV) Size focusing: $Au_{40}(SR)_{26} \rightarrow Au_{36}(SR)_{24} + 2Au(0) + 2\ Au(I)SR$

Given the implications from the LEIST reaction for nanoclusters, it is expected that the larger nanoparticles should have a similar transformation process during the ligand exchange, although it may be difficult to be observed. Nevertheless, there are a few reports on the phase transformation of nanoparticles when the surrounding environment is changed. For example, gold square sheets with a hexagonal-close-packing (HCP) phase can be transformed into a FCC phase by the ligand exchange process [37]. Also, Banfield and coworkers reported that the binding of water molecules to the 3 nm ZnS nanoparticles leads to a dramatic structural modification from the surface to interior [38]. In both nanocluster and nanoparticle transformations, the ligand-exchange processes introduce stress on the surface, which further propagates into the core and leads to the entire structure transformation.

The precise nanoscale reactions should not be limited to the LEIST case. It is expected that other factors which stimulate nanoscale transformation, can be exploited to develop into systematic "induced size/structure transformation (IST)" methodologies. For example, a metal-exchange process has recently been reported to transform an $Au_{23}(S\text{-}c\text{-}C_6H_{11})_{18}$ nanocluster into an $Ag_xAg_{25-x}(S\text{-}c\text{-}C_6H_{11})_{18}$ nanocluster [39], and a systematic "MEIST" reaction may be developed. Other processes, such as oxidation (OIST) [40], reduction (RIST), photoinduction (PIST), etc., may also lead to the transformations. It would be exciting to explore more precise transformation pathways of nanomaterials for achieving the goal of rational design and controlled synthesis of complex nanostructures.

## Phases: from bulk to nanocluster

How the atoms are packed inside the nanocrystals and how the structures evolve as a function of size is a fundamental issue in nanoscience. The phases of nanocrystals may be different from their bulk counterparts, because of nanocrystals are confined in a limited space and the surface can significantly affect the total energy minimization. Bulk gold adopts a face-centered cubic (FCC) packing with a lattice parameter ($a$) of 4.080 Å and an Au–Au distance of $d = a/\sqrt{2} = 2.885$ Å. The phases of gold nanocrystals are more diverse, e.g. the cases characterized by multiple twinning planes [41]. The 20-fold twinned, the five-fold twinned and single crystalline phases were frequently observed in gold nanocrystals by TEM [42–45]. Scheme 4 provides a demonstration of how 55 gold atoms can be assembled in different ways to form the icosahedron, decahedron, and cuboctahedron with various twinning planes and facets.

Theoretical modeling has shown that the stabilities of these three phases are different as a function of size, with icosahedron (Ih) being stable for the smaller nanocrystals, decahedron (Dh) for the medium sizes and cuboctahedron (or FCC) for the larger sizes [46, 47]. Such a trend is a result of the interplay between the "volume energy" and the "surface energy" of a polyhedron. The volume energy decreases as Ih > Dh > FCC, since the incorporation of twining planes in the phase increases the volume energy (Scheme 4b). On the other hand, the surface energy increases as Ih < Dh < FCC, because the Ih is exclusively terminated with low-energy {111} facets while the cuboctahedron is terminated with a mix of {111} and the higher energy {100} facets (Scheme 4c). As the size of nanoparticle as well as the volume to surface ratio increases, the volume energy outweigh the surface energy. Therefore, the single crystalline FCC phase is favored for the larger size, while the multiple-twinned icosahedral phase is favored for the smaller sizes.

The first three structures discovered in $Au_n(SR)_m$ nanoclusters indeed follow this stability trend. The smaller $Au_{25}(SCH_2CH_2Ph)_{18}$ has an $Au_{13}$ icosahedral kernel [48, 49] and $Au_{38}(SCH_2CH_2Ph)_{24}$ has an $Au_{23}$ face-sharing bi-icosahedral kernel [50]. When going to the larger $Au_{102}(p\text{-MBA})_{44}$, an $Au_{79}$ decahedral kernel is observed [51]. However, this neat trend was broken when the $Au_{36}(TBBT)_{24}$ structure was discovered [31].

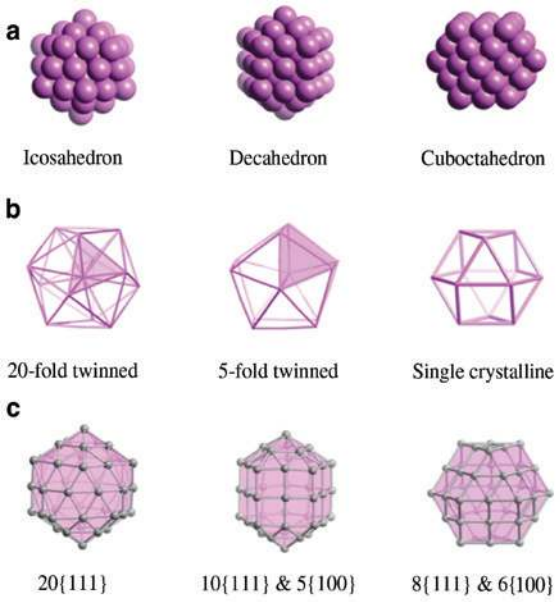


**Scheme 4:** Phases frequently observed in gold nanocrystals. (a) Model of 55 gold atoms packed into an icosahedron, Ino decahedron and cuboctahedron. (b) Different twinning in the three phases. (c) Different facets on the surfaces of the three phases.

Despite its smaller size, $Au_{36}(TBBT)_{24}$ has a single crystalline FCC kernel with 28 core gold atoms packed into a truncated tetrahedral shape. The discovery of FCC kernel in $Au_{36}(TBBT)_{24}$ as well as the above-mentioned ligand-induced transformation of the structures of nanoclusters indicates that the surface-protecting molecules play a pivotal role in dictating the packing of gold atoms inside the kernel. Moreover, the stability trend is completely broken as more and more crystal structures are discovered recently [52]. The gold nanocluster structures are found to be much more diverse than their larger counterparts. New phases such as body-centered cubic [53] and hexagonal close packing [54] are also observed.

The break of stability trend in the ligand-protected nanoclusters is reasonable, since the theoretically predicted trend is based on bare clusters without consideration of surface binding molecules. The surface energy of the ligand-protected nanoclusters not only includes the facet's energy, but also consists of the binding energy between metal atoms and the functional groups of ligands as well as the intermolecular interactions among the carbon tails (vide infra). Incorporation of the latter two terms is expected to give a more precise prediction of the stability trend, but it would also require a significant increase in computational power and time. Below we provide three examples of phases observed in large gold nanoclusters, which are also important for the discussion of surface structure in the next section.

Figure 2 shows the FCC kernel structure in $Au_{92}(TBBT)_{44}$ [55]. The 84 gold atoms are packed in a layer-by-layer manner into a $6 \times 6 \times 5$ FCC lattice along the three <100> directions, which corresponds to the six (100) layers, six (010) layers, and five (001) layers along the *x*-, *y*-, and z-axis, respectively (Fig. 2a). A total of 90 gold atoms are required to assemble into this $1.05 \times 1.05 \times 0.84$ $nm^3$ nanocrystal. Further truncation of two columns of atoms at two edges along the *z*-axis (Fig. 2a, gray balls) leads to the final $Au_{84}$ kernel. This tetragonal shaped kernel exposes six pieces of well-defined {100} facets, which provide a unique opportunity to study the surface structures of the self-assembled monolayer of thiolates on Au(100) facets (vide infra).

Protected by the same TBBT ligands, the $Au_{133}(TBBT)_{52}$ nanocluster exhibits a 20-fold twinned icosahedral kernel (Fig. 3) different than the FCC kernel in $Au_{92}(TBBT)_{44}$ [33]. The kernel is assembled from 107 gold atoms in a shell-by-shell manner with a central gold atom surrounded by 12, 42, and 52 gold atoms in the shells successively (Fig. 3a–c). While the first two shells are assembled into a perfect 55-atom Mackay icosahedron with an a-b-c packing mode (Fig. 3d,e) [56], the third shell serves as a transition layer between

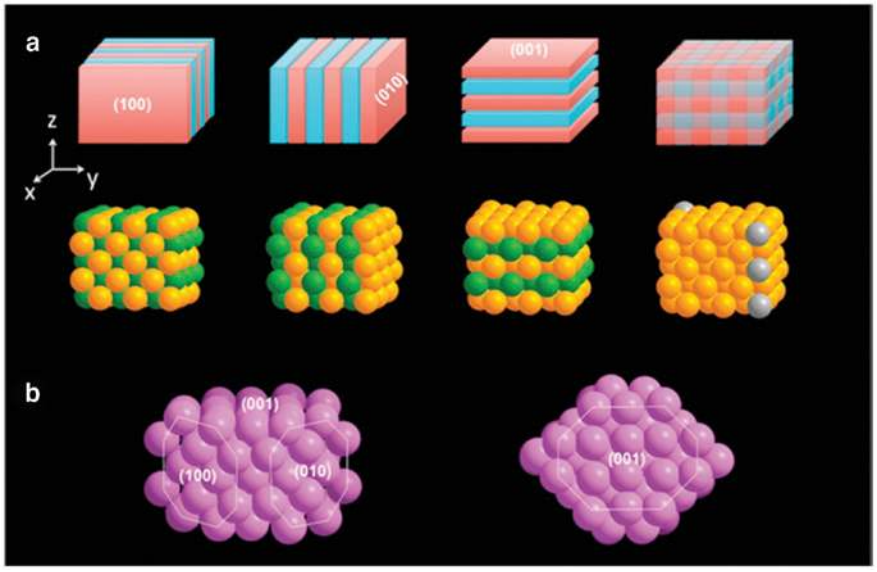


**Fig. 2:** Single crystalline FCC phase in the $Au_{92}(TBBT)_{44}$ nanocluster. (a) Structural models of the gold kernel. (b) The 84 gold atoms in $Au_{92}(TBBT)_{44}$ pack into a piece of single crystalline with well-defined shape and crystalline {100} facets. Adapted with permission from Ref. [55].

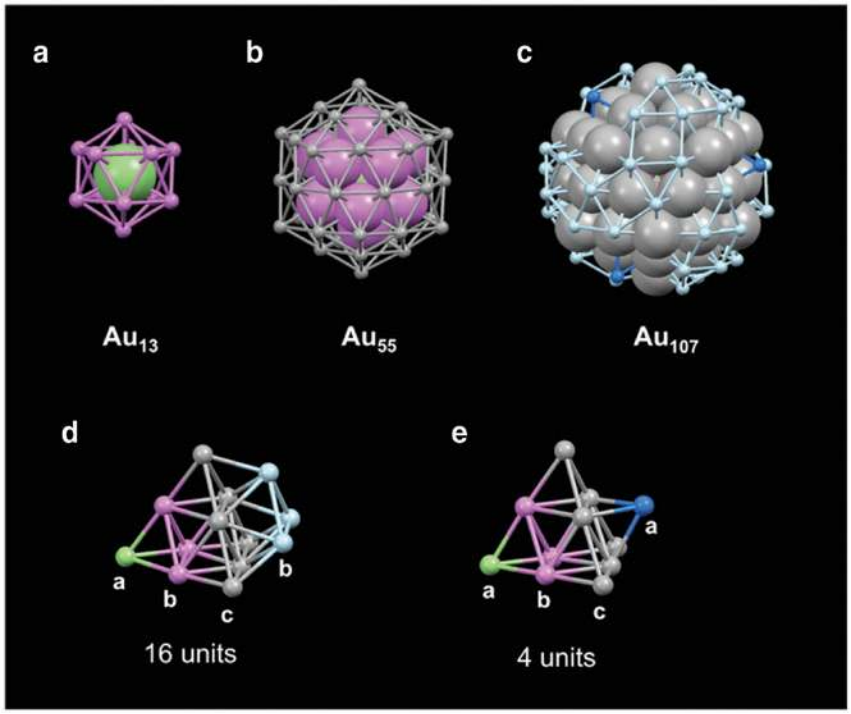


**Fig. 3:** The 20-fold twinned $Au_{107}$ icosahedral kernel in the $Au_{133}(TBBT)_{52}$ nanoclusters. (a) The first icosahedral shell with 12 Au atoms (pink). (b) Second icosahedral shell with 42 Au atoms (gray) (c) third transitional shell with 52 Au atoms (blue and cyan). (d) a-b-c-b packing of gold atoms in 16 tetrahedral units of an icosahedron. (e) a-b-c-a packing of gold atoms in the remaining 4 tetrahedral units. Adapted with permission from Ref. [33].

the polyhedron and the surface layer and breaks the symmetry of the icosahedron. The radial Au–Au bond lengths ($r = 2.760 \pm 0.008$ Å) and the transverse bond lengths ($t = 2.920 \pm 0.035$ Å) match closely with the geometric requirement of an icosahedron, which is $r = 0.95t$.

Figure 4 provides an example of 5-fold twinned decahedral kernel in a "giant" 2.2 nm $Au_{246}(p\text{-MBT})_{80}$ nanocluster [57]. The decahedral $Au_{206}$ kernel is constructed in a similar shell-by-shell manner as the $Au_{107}$ kernel in $Au_{133}(TBBT)_{52}$. The first three shells assemble into an $Au_{116}$ Ino decahedron with five twinning planes, ten {111} facets, and five {100} facets. The fourth shell is a transitional layer, which has multiple roles: (i) rounds the inner polyhedron, (ii) lowers the surface energy, and (iii) provides the anchoring points for the surface-protecting thiolates.

From these three examples, we can see that the phases of nanoclusters are highly diverse and are both size-dependent and ligand-dependent. For the same type of ligand, different phases can be observed with different sizes, e.g. FCC in $Au_{92}(TBBT)_{44}$ and icosahedron in $Au_{133}(TBBT)_{52}$. Also, nanoclusters can adopt different phases in a similar size range by varying the surface ligands, as demonstrated in the decahedral kernel in $Au_{130}(p\text{-MBT})_{50}$ and icosahedron in $Au_{133}(TBBT)_{52}$ [35].

## Surfaces: from single motifs to ensemble patterns

The surface is a crucial part of nanoparticles, but it is the most difficult to characterize. The gold-thiolate interfaces, either as self-assembled monolayers (SAMs) on the extended gold crystalline surface or as a monolayer on the nanoparticle surface, are considered as a platform of nanotechnology and are widely applied in lithography, electronic devices, biomedicine, etc., [58]. The gold-thiolate interfaces have been extensively studied for about three decades [59, 60], but the atomic structure of SAMs is still not conclusive. The total structure determination of nanoclusters provides some atomic-level insights into the SAM structure. For example, the monomeric staple motifs (e.g. –S–Au–S–) discovered in $Au_{102}(SR)_{44}$ nanocluster [51] has been applied to support the gold adatom binding modes on the SAMs [61, 62].

A comprehensive understanding of surface structure can be more challenging than the core structure since the surface is a more complex system and contains multiple parts. Generally speaking, the total structure of the surface includes (i) the binding geometry between the ligands and the exposed inorganic atoms on the substrate, and (ii) the patterning symmetry of ligands on the extended area (Scheme 5). The binding geometry can be further divided into three levels: (i) the underlying atomic lattice (whether it is alternated by surface binding or not); (ii) the binding between the functional groups of ligands and the atoms in the substrate lattice; (iii) the orientation of carbon chains. In addition, there are different types of surfaces, including curved surface or planar crystalline surface (Scheme 5a); the (111) or (100) surface (Scheme 5c); and vertex, edge or facet of a nanoparticle (Scheme 5b). Therefore, one should be careful to project the surface structures

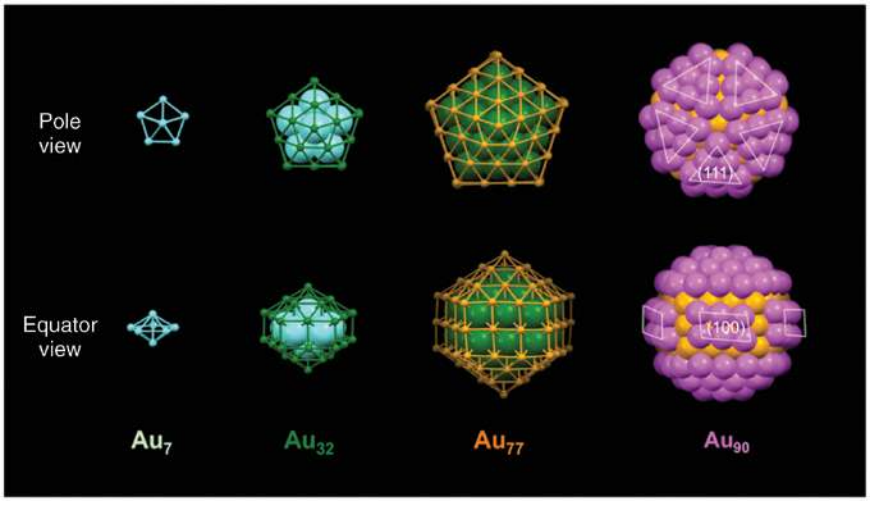


**Fig. 4:** The five-fold twinned $Au_{206}$ decahedral kernel in the $Au_{246}(MBT)_{80}$ nanoclusters. Adapted with permission from Ref. [57].

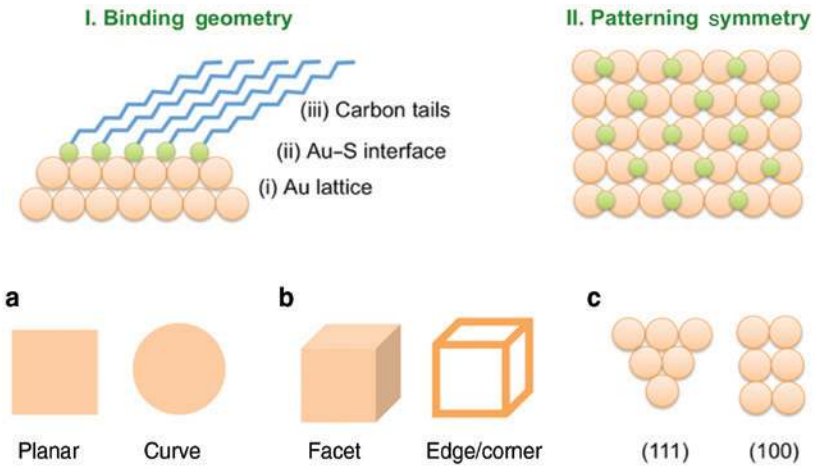


**Scheme 5:** Total structures of the two-dimensional surface, which includes the binding geometry and the patterning symmetry in different environments. (a) Planar surface vs. curved surface. (b) Facet vs. edge and corner. (c) (111) Surface vs. (100) surface.

discovered in one system to another. Fortunately, many $Au_n(SR)_m$ structures have been identified in recent years, which can cover most cases of surface structures.

The earlier work has been focused on the elucidation of gold-thiolate binding structures as a function of nanocluster size [63–66]. Instead of simply adsorbing on the gold surface, thiolates together with gold atoms tend to form the oligomeric "staple-like" motifs (Fig. 5). This is demonstrated in the monomeric staple motifs (–S–Au–S–) in $Au_{102}(SR)_{44}$ [51], dimeric staple motifs (–S–Au–S–Au–S–) in $Au_{38}(SR)_{24}$ and $Au_{25}(SR)_{18}$ [48–50], trimeric motifs in $Au_{23}(SR)_{16}$ [67], tetrameric motifs in $Au_{24}(SR)_{20}$ [68, 69], etc. A general trend is that as the size of nanocluster decreases, longer staple motifs are required, in order to accommodate the increasing surface curvatures of the smaller nanoclusters. Interestingly, the staple motif eventually closes up and evolves into an octameric ring motifs in the ultrasmall $Au_{20}(TBBT)_{16}$ nanocluster (Fig. 5 bottom) [70]. This ring motif protects the inner $Au_7$ "bowtie" kernel via Au(I)–Au(I) aurophilic interactions.

While the diverse binding motifs are revealed in the smaller $Au_n(SR)_m$ nanoclusters, it requires the larger nanoclusters to further demonstrate the packing symmetry of ligands on the extended Au surface. It is first demonstrated in the $Au_{133}(TBBT)_{52}$ nanocluster that surface binding motifs can self-assemble into large-scale, symmetric and esthetic patterns [33]. As shown in Fig. 6, the icosahedral $Au_{107}$ kernel in the $Au_{133}(TBBT)_{52}$ nanocluster (Fig. 3) is exclusively protected by 26 of the monomeric staples (–S–Au–S–); among them, 24 of such staple motifs self-assemble into four "helical stripes", which coil up around the globular kernel from one

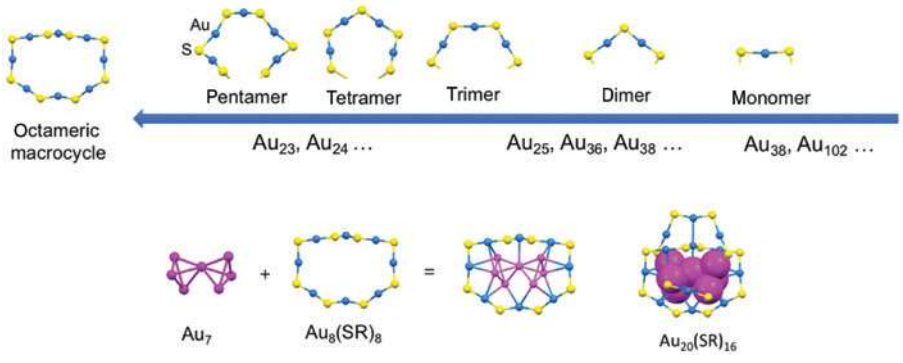


**Fig. 5:** Evolution of surface protecting motifs in $Au_n(SR)_m$ nanoclusters. As the sizes of nanoclusters decreasing, longer $Au_x(SR)_{x+1}$ staple motif appears, which further evolves into an octameric macrocycle in the ultrasmall $Au_{20}(SR)_{16}$ nanocluster. Adapted with permission from Ref. [70].

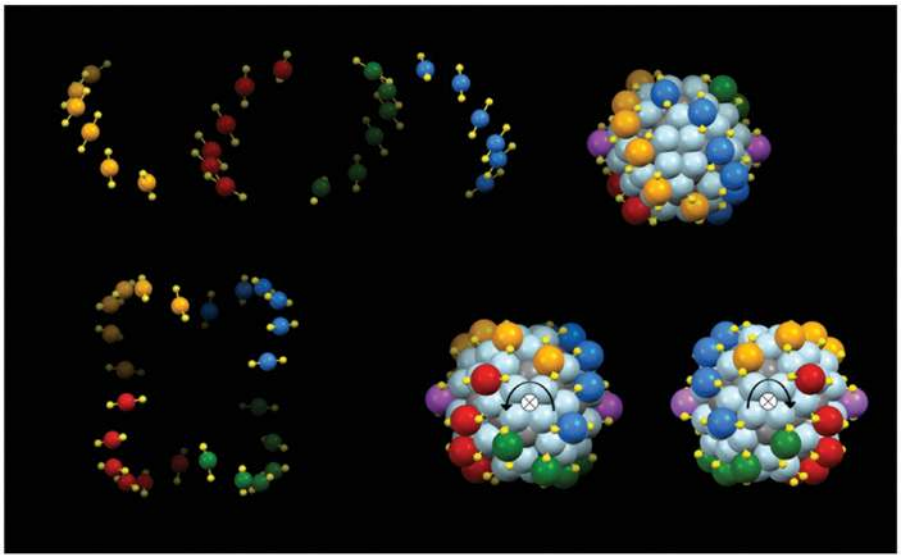

**Fig. 6:** Self-assembled monolayers on the curved surface of $Au_{133}(SR)_{52}$ nanoclusters. Adapted with permission from Ref. [33].

pole to the other pole like a four-leaf clover. The clockwise or anticlockwise assembly of four helices bestows chirality to the $Au_{133}(TBBT)_{52}$ nanocluster. Such a parallel alignment of (–S–Au–S–) into helical stripes on the curved surface is in contrast with the rectangular stripes observed in the planar gold surface [61, 62]. Interestingly, when the shape of the kernel changes from a sphere in $Au_{133}(TBBT)_{52}$ to a barrel in $Au_{130}(p\text{-MBT})_{50}$, the self-assembled surface –S–Au–S– pattern changes from four-fold helixes to five-fold "ripples" [35].

Most of the identified gold nanoclusters have curved surfaces without exposing of extended planar facets. Therefore the surface patterns observed in those nanoclusters may not be good representatives to the gold crystalline surfaces such as Au(111) and Au(100), which are the typical substrates for the self-assembled monolayers (SAMs). A recent achievement (i.e. the $Au_{92}$ structure) offers an excellent model for the (100) SAM structure [55]. The layer-by-layer assembly of gold atoms in the kernel of $Au_{92}(TBBT)_{44}$ enables a faster growth of crystalline facet compared with the shell-by-shell assembly. As shown in Fig. 7, the highly regular tetragonal $Au_{84}$ kernel in $Au_{92}(TBBT)_{44}$ (Fig. 2) exposes the hitherto largest {100} facet (i.e. 16 gold atoms) observed in the gold nanoclusters. Significantly, the thiolates adopt the same binding geometry (i.e. bridging mode) as well as patterning symmetry (i.e. square symmetry) on all of the six exposed Au{100} facets (Fig. 7a). Because of the translational symmetry, these pieces of "nanoSAMs" on nanocluster surface can be further generalized to the bulk Au{100} SAMs. The thiolates simply bridge on the Au{100} plane (Fig. 7c). The underlying gold lattice is slightly distorted due to the bridging-mode effect of the thiolates, with the Au–Au bonds beneath the sulfur bridges being stretched, while the adjacent Au–Au bonds being contracted (Fig. 7b). The carbon tails of the thiolates are parallelly aligned (Fig. 7d).

Other than the facets, the $Au_{92}(TBBT)_{44}$ nanocluster also provides an opportunity to exam the protecting modes of thiolates on the edges and corners. The edge is protected by –S–Au–S– monomeric staple motifs, which can be actually be viewed as 2 bridging thiolates at 2 connecting facets joined by one gold atom at the edge. Similarly, the corner is protected by –S–Au–S–Au–S– dimeric staple motif, which can be viewed three simple bridging thiolates at the three facets joined by the two corner gold atoms. The monomeric and dimeric staple motifs at the edges and corners are very similar to the motifs that protect the curved surface.

Compared to Au{100} surface, Au{111} surface is a more common substrate for SAMs. The largest Au{111} facets of gold nanoclusters is discovered by Chen et al. in the $Au_{40}(o\text{-MBT})_{24}$ structure [34, 75]. Similarly, the gold lattice in $Au_{40}(o\text{-MBT})_{24}$ is built up along the <111> direction to form a hexagonal plate. The layer-by-layer growth fashion allows this tiny cluster to expose two large 12-gold-atom Au{111} facets at the bases of the plate [75]. The thiolates also adopt simple bridging modes on the Au{111} facets, with the six -S- bridges give a full protection of the 12 gold atoms. However, the thiolates assemble with a three-fold rotational symmetry

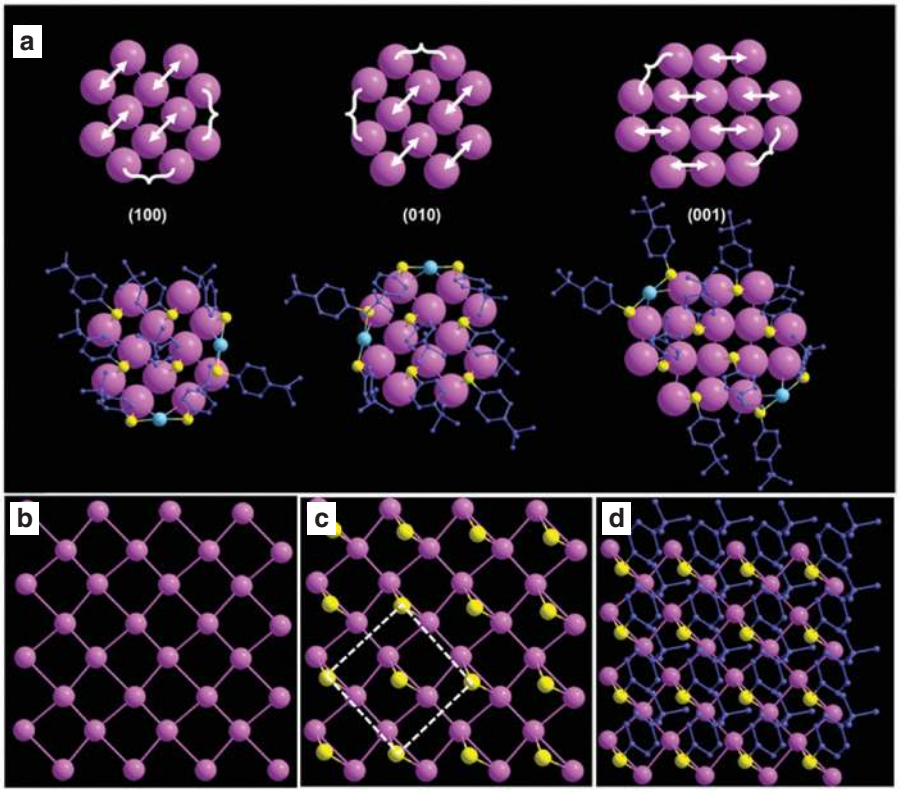


**Fig. 7:** Structure of self-assembled monolayers of thiolates on the planar Au {100} facets. (a) Structures of NanoSAMs observed in the $Au_{92}(TBBT)_{44}$ surface. (b–d) Extended SAMs structure generalized from the nanoSAMs, including the distortion of the underlying gold lattice (b), binding at the gold-thiolate interface (c) and orientation of carbon tails. Adapted with permission from Ref. [55].

instead of a long-range translational symmetry. Therefore, the patterning symmetry of bulk Au{111} SAMs cannot be represented from the Au{111} nanoSAMs in $Au_{40}$(*o*-MBT)$_{24}$. One major difference between bulk SAMs and nanoSAMs observed in the nanoclusters is that the latter requires a full protection of the substrate atoms while the former does not.

## Periodicity: a series of gold quantum boxes

How the properties of nanoclusters evolve as their size increases is another important question [71]. Many "magic sizes" (i.e. stable sizes) of $Au_n(SR)_m$ nanoclusters have been discovered in recent years and some structures are identified by X-ray crystallography (Scheme 6a) [52]. It is possible to make every number ($n$) a "magic size" by applying different types of thiolates ligands with a fine control of reaction conditions (Scheme 6b). At the early stage of the structure identification, each $Au_n(SR)_m$ structure comes out as a surprise, and there are no clear structure evolution rules as a function of size. Also, the properties of the nanoclusters are not simply size-dependent [72]. For example, the band gaps of nanoclusters fluctuate instead of decreasing monotonously with increasing size: $Au_{25}(SR)_{18}$ has a band gap of 1.3 eV; but the band gap of $Au_{36}(SR)_{24}$ increases to 1.7 eV instead of the expected decrease with increasing size; when coming to $Au_{38}(SR)_{24}$, the gap drops back to 0.9 eV. The fluctuation in properties is because the properties of nanoclusters are not only dependent on the size, but also dependent on the structures and ligands.

As more and more sizes and structures of nanoclusters are identified, we indeed discover that akin to the atoms in the periodic table, periodicity is existed in some nanoclusters [73]. This is demonstrated in a "magic series" of gold nanoclusters including $Au_{28}(TBBT)_{20}$ [32], $Au_{36}(TBBT)_{24}$ [31], $Au_{44}(TBBT)_{28}$ [74], and

a

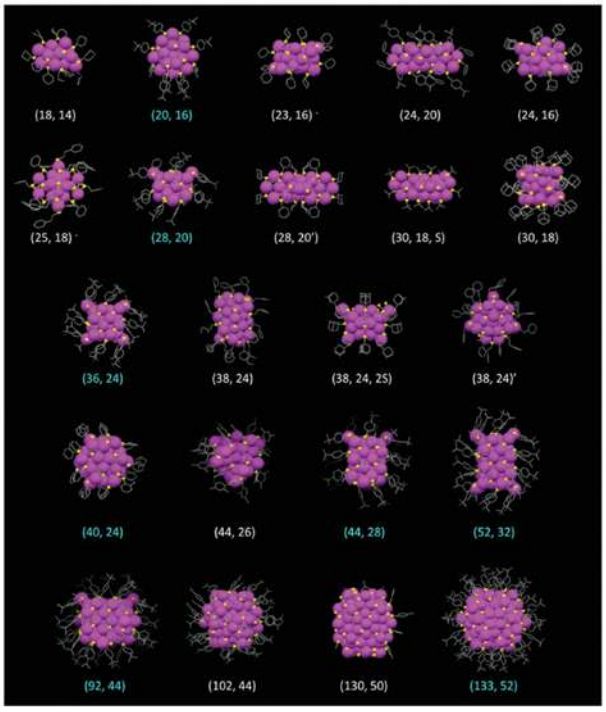


b

$n$ =

| | | | | | | | | | |
|---|---|---|---|---|---|---|---|---|---|
| | | | | | | | | | 10 |
| | 12 | | | 15 | | | 18 | | 20 |
| | 22 | 23 | 24 | 25 | | | 28 | | 30 |
| | | | | | 36 | | 38 | | 40 |
| | | | 44 | | | | | | |
| | 52 | | | | | | | | |
| | | | 64 | 65 | | | | | |
| | | | | | | | | | |
| | | | | | | | | | |
| | 92 | | | | | | | 99 | |
| | 102 | | 104 | | | | | | |
| | | | | | | | | | |
| | | | | | | | | | 130 |
| | | 133 | | | | 137 | | | |
| | | | 144 | | | | | | ... |

**Scheme 6:** (a) The atlas of gold nanocluster structures published by Nov 2016. ($n$, $m$) represents $Au_n(SR)_m$. The nanoclusters discussed in this work are highlighted as blue. Magenta = gold, yellow = sulfur, gray = carbon. Redrawn from the cif files of the nanoclusters [52]. (b) A table listing the identified $Au_n(SR)_m$ nanoclusters.

$Au_{52}(TBBT)_{32}$ [75] (Fig. 8a). The periodicity is first demonstrated in a unified formula of $Au_{8x+4}(SR)_{x+8}$, with $x = 3, 4, 5, 6$ for the four sizes, respectively. The periodicity in formulas is actually a reflection of the uniform layer-by-layer growth pattern of the nanoclusters along the [100] direction of the FCC lattice (Fig. 8b). Significantly, the overall formula of $Au_{8x+4}(TBBT)_{4x+8}$ can be precisely correlated with their structure evolution: the "$x$" represents the number of (001) layers in the FCC kernel; the "$8x$" indicates that each additional (100) layer contains eight gold atoms; the "$4x$" reflects that 4 more bridging thiolates are required with each addition of (100) layer; and the starting $Au_4(TBBT)_8$ represents the initial four $Au(SR)_2$ staple motifs located at the edges of the nanoclusters (Fig. 8b).

The periodicity in size and structure leads to a uniform evolution of the optical properties in the $Au_{8x+4}(SR)_{4x+8}$ nanoclusters. As shown in Fig. 8c, the UV-vis absorption spectra of these nanoclusters exhibit similar profiles, with an intense peak at ~400 nm, and a weaker plateau in the near IR region. As the size increases from $Au_{28}$, $Au_{36}$, $Au_{44}$, to $Au_{52}$, the ~400 nm slightly redshifts from 366 to 376, 380, and 396 nm, and the onset of near IR plateau redshifts significantly from 702 to 704, 820, and 890 nm, which corresponds to Eg = 1.77, 1.76, 1.51, 1.39 eV, respectively. The similar absorption profiles are due to the same structural patterns among the four sizes, and the monotonous redshift of band gap corresponds to the anisotropic growth of the nanoclusters.

Interestingly, this series of nanoclusters serves as a nice model for the three-dimensional "quantum boxes", similar to other well-defined quantum systems such as one-dimensional conjugated alkenes [76] or three-dimensional semiconductor quantum dots [77]. Intuitively, their optical properties can be explained by solving the Schrödinger equation for a 3D "particle in a box" model (eq. 1). The dimension of these quantum boxes can be defined by $a$, $b$ and $c$, with $a = b = 0.6$ nm, and $c = 0.2\,l$ nm ($l = 2$–$5$ for the four sizes, respectively). Based on such a quantum box model, the energy levels of the magic series can be calculated by the equation:

$$E = \frac{h^2}{8m}\left(\frac{n_x^2}{a^2} + \frac{n_y^2}{b^2} + \frac{n_z^2}{c^2}\right) \quad (1)$$

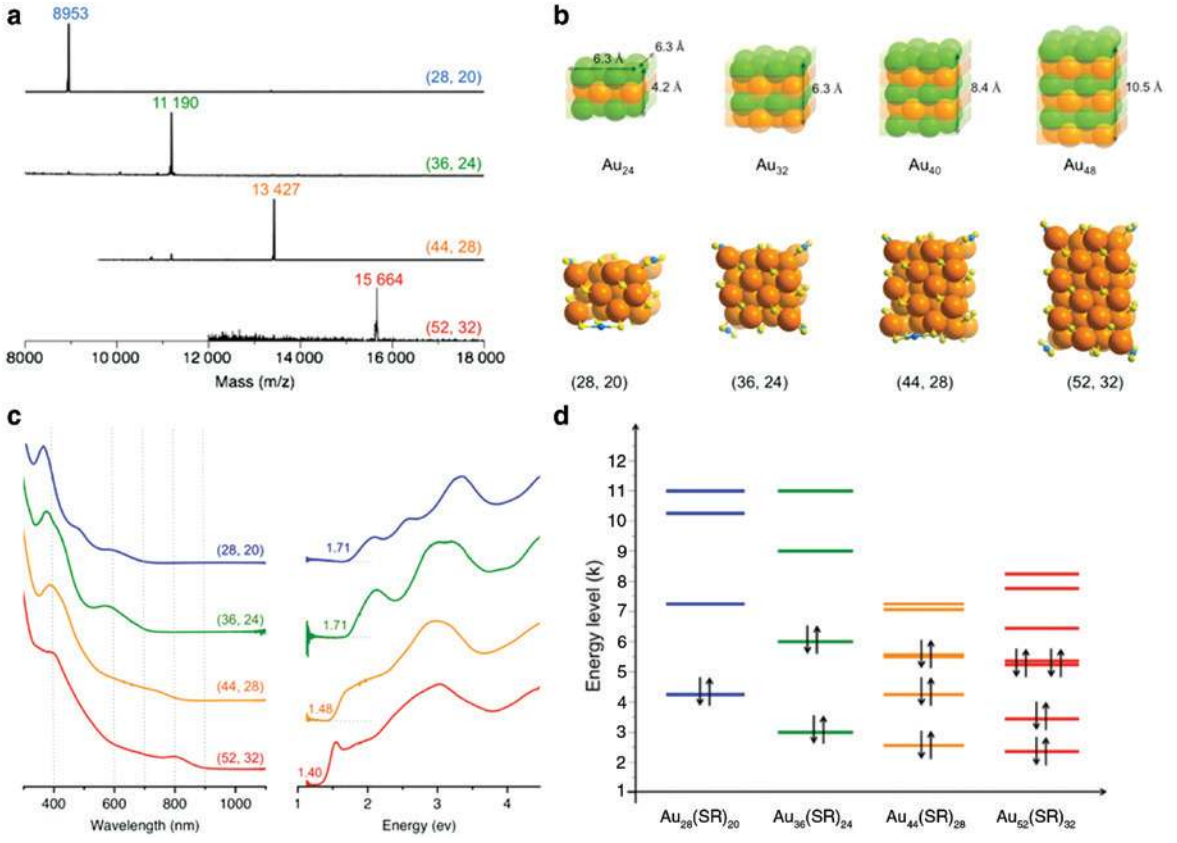


**Fig. 8:** Periodicities in the size, structure, and optical property of a series of $Au_{8x+4}(SR)_{4x+8}$ nanoclusters ($x = 3–6$). (a) Electrospray ionization mass spectra. (b) Structure of Au kernel and gold-thiolate framework in the series. (c) UV-vis absorption spectra in wavelength scale and energy scale. (d) Energy levels of the nanoclusters calculated by the 3D "particle-in-a-box" model. Adapted with permission from Ref. [73].

By plugging into the dimensions of the box (i.e. $a = 0.6$ nm, $b = 0.6$ nm, $c = 0.2l$ nm), the equation is re-written as:

$$E = k\left(n_x^2 + n_y^2 + \frac{9}{l^2}n_z^2\right), \text{ where } k = \frac{h^2}{8m(0.2\times 3\times 10^{-9})^2} \tag{2}$$

Then the energy level distribution of each nanocluster can be calculated by varying the $n_x$, $n_y$ and $n_z$ values (as shown in Table 1). The quantized energy levels are drawn in Fig. 8d based on Table 1.

**Table 1:** Quantized energy levels calculated based on the 3D "particle in a box" model.

| | $Au_{28}(TBBT)_{20}$ | $Au_{36}(TBBT)_{24}$ | $Au_{44}(TBBT)_{28}$ | $Au_{52}(TBBT)_{32}$ |
|---|---|---|---|---|
| | $E = k(n_x^2 + n_y^2 + 9/4\, n_z^2)$ | $E = k(n_x^2 + n_y^2 + n_z^2)$ | $E = k(n_x^2 + n_y^2 + 9/16\, n_z^2)$ | $E = k(n_x^2 + n_y^2 + 9/25\, n_z^2)$ |
| $E_1$ | 4.25k: (111) | 3k: (111) | 2.56k: (111) | 2.36k: (111) |
| $E_2$ | 7.25k: (211) (121) | 6k: (211)(121)(112) | 4.25k: (112) | 3.44k: (112) |
| $E_3$ | 10.25k: (221) | 9k: (122)(221)(212) | 5.56k: (211)(121) | 5.24k: (113) |
| $E_4$ | 11k: (112) | 11k: (113) | 7.06k: (113) | 5.36k: (211) (121) |
| $E_5$ | | | 7.25k: (212)(122) | 6.44k: (212) (122) |
| $E_6$ | | | 8.56k: (221) | 7.76k: (114) |
| $E_7$ | | | | 8.24k: (213) |

The final step is to fill the quantized energy levels with electrons. To simplify the case, only the 6s electrons of gold atoms in the central part (without bonding to any thiolate) are considered to fill the quantum box energy levels (i.e. 2e, 4e, 6e, and 8e for the four sizes, respectively). This gives rise to energy gaps $\Delta E = 3k$, 3k, 1.5k, 1.08k for the four sizes, respectively (Fig. 8d). This simple model partially explains the size-dependent energy gaps, and why the $Au_{28}$ and $Au_{36}$ have nearly the same band gaps.

It is possible that such a periodic series of $Au_{8x+4}(SR)_{4x+8}$ nanoclusters can be further extended to $x = 7$, 8, 9, 10, etc. But increasing of anisotropy during the growth of nanoclusters would make them more challenge to be synthesized. Theoretical calculations have provided some insights on the further evolution of the properties of this periodic series [78, 79]. It is worth noting the formula of $Au_{20}(TBBT)_{16}$ also falls into the magic series (i.e. $x = 2$), but its structure does not follow the layer-by-layer growth mode. Instead, $Au_{20}(TBBT)_{16}$ has a core-shell structure as shown in Fig. 5. It would be exciting to identify more periodic series, for example, nanoclusters with a (111) cross sections during layer-by-layer growth. Such a periodicity would further facilitate a systematic understanding of the structure-property correlations in nanoclusters.

## Assembly: emergence of hierarchical structural complexities

Hierarchical self-assembly is an essential process adopted by nature to spontaneously create complex structures from molecules, cells to living organisms. Therefore, it is important for chemists to understand the self-assembly process and the intermolecular interactions in order to build up more complex and functional architectures across the nanoscale. In this part, we provide an example that the synthetic nanoparticle systems can achieve a similar level of precision, hierarchy, and complexity as biological system during the self-assembly process, as demonstrated in the $Au_{246}(p\text{-MBT})_{80}$ nanocluster [57]. The self-assembly processes in the nanoparticle system involve three different length scales: (i) assembly of the inorganic atoms at the atomic scale, (ii) assembly of surface ligands at the molecular scale, and (iii) assembly of the nanoparticles at the nanoscale. Among these three levels of assemblies, we found that the self-assembly of surface ligands at the molecular scale is the most crucial and largely dictates the inter-particle and intra-particle self-assembly processes (Fig. 9).

The self-assembly of the surface protecting *p*-MBT ligands in $Au_{246}(p\text{-MBT})_{80}$ is governed by the intermolecular C–H$\cdots\pi$ interactions, in which the $\pi$ electrons of the phenyl rings interact with C–H bonds from methyl groups or phenyl rings (Fig. 10g). Twenty five of the *p*-MBT ligands assemble into a five-fold rotational pattern via C–H$\cdots\pi$ interactions at each pole site of the gold sphere, with a density of ~14 ligands nm$^{-2}$

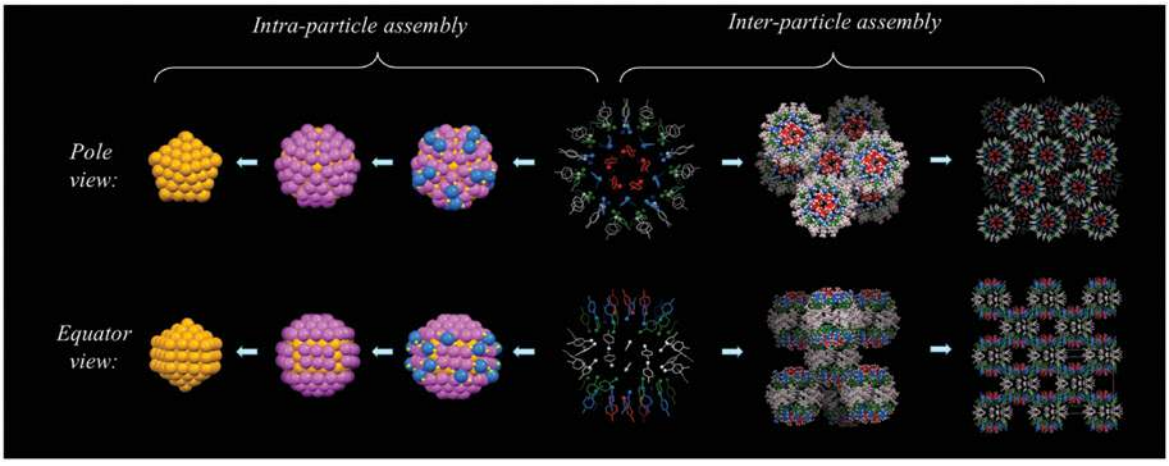


**Fig. 9:** The self-assembled surface ligands dictate the intraparticle and interparticle assembly of $Au_{246}(p\text{-MBT})_{80}$ nanoparticles. Adapted with permission from Ref. [57].

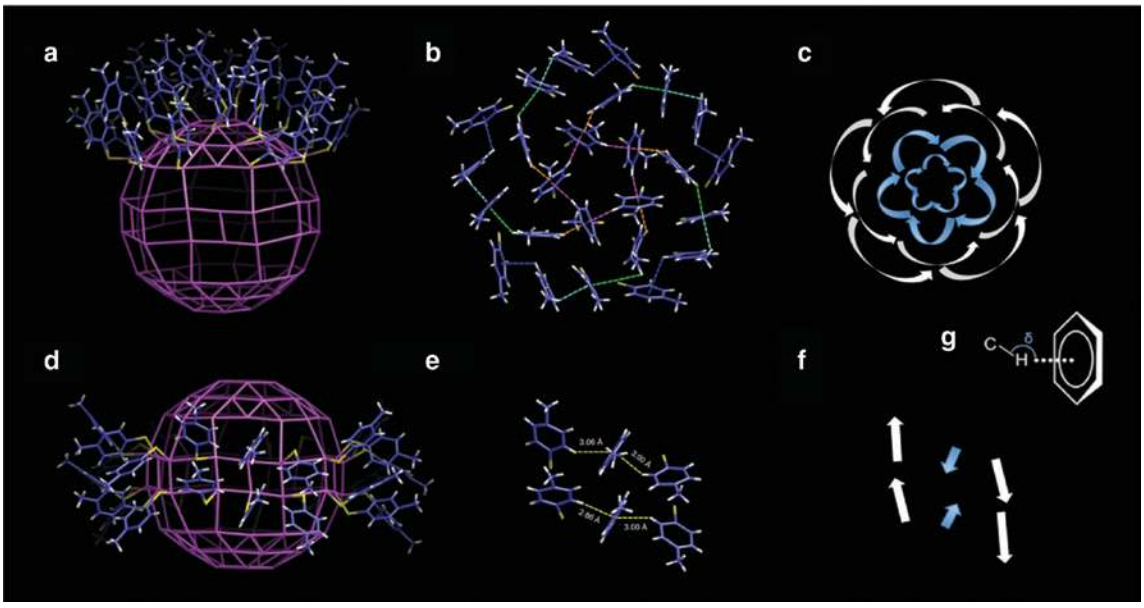


**Fig. 10:** Self-assembly of *p*-MBT ligands via C–H · · · π interactions on the pole and equator of the gold sphere. (a–c) Assembly on the pole. (d–e) Assembly on the equator. (g) Scheme for C–H · · · π interactions. Adapted with permission from Ref. [57].

(Fig. 10a–c). At the equator, 30 of *p*-MBT ligand assemble parallelly into alternating pairs with a density of ~6 ligands $nm^{-2}$ (Fig. 10d–f). The individual C–H · · · π interaction is relatively weak with a strength of about 1.5–2.5 kcal/mol [80, 81], but the collective C–H · · · π interactions in the large-scale surface patterns can be quite strong and can generate an energy barrier to stabilize the pattern. Indeed, the rotational and parallel patterns of the surface ligands are reminiscent of the α-helix and β-sheet in the secondary structures of proteins, which are stabilized by hydrogen bonds.

Through the weak intermolecular interactions, the thiolate ligands assemble into different patterns on the gold surface, and these surface patterns further serve as "interaction motifs" to guide the next level of assembly of nanoclusters. Two surface features are responsible for the assembly of nanoclusters into ordered single crystals. The first one is the maximization of interactions, in which the nanoclusters contact with each other through the more densely packed rotational patterns at the pole site. In this way, the van der Waals interactions among the nanoclusters are maximized. The second one is the matching of the symmetry between different surface patches. A more detailed examination of the contacting areas of the two nanoclusters shows that the surface rotational patterns are attached to each other through the regions with the same symmetry, which further facilitates the interlocking of the nanoclusters. The self-assembly of ligands and nanoclusters demonstrates the emergence of hierarchical interactions to build up more complex structures across different length scales.

The emergent behavior also helps to explain the complex relationship between the surface ligands and the core structures. The small difference of thiolate ligands, such as *p*-TBBT vs *p*-MBT, through self-assembly, can be amplified to affect the total structure of nanoparticles [35]. The *p*-MBT ligands have the tendency to be packed into a five-fold symmetry (Fig. 11a), which is further manifested in the packing at gold-thiolate interface as well as in the five-fold decahedron kernel. In contrast, due to the bulkiness of the tert-butyl group, the *p*-TBBT ligands adopt a four-fold rotational packing (Fig. 11b). This initial symmetry leads to the orientation of the surface staple motifs into the four helixes at the Au-S interface, which further affect the symmetry of the transitional layer and finally select the 20-fold twinned icosahedral kernel (Fig. 11b). We note that the $C_2$ rotational axes in the icosahedron are commensurate to the initial four-fold symmetry. Such an observation of "small change results in big difference" and the hierarchical structural adaptation are the key features of the emergence phenomenon [82, 83].

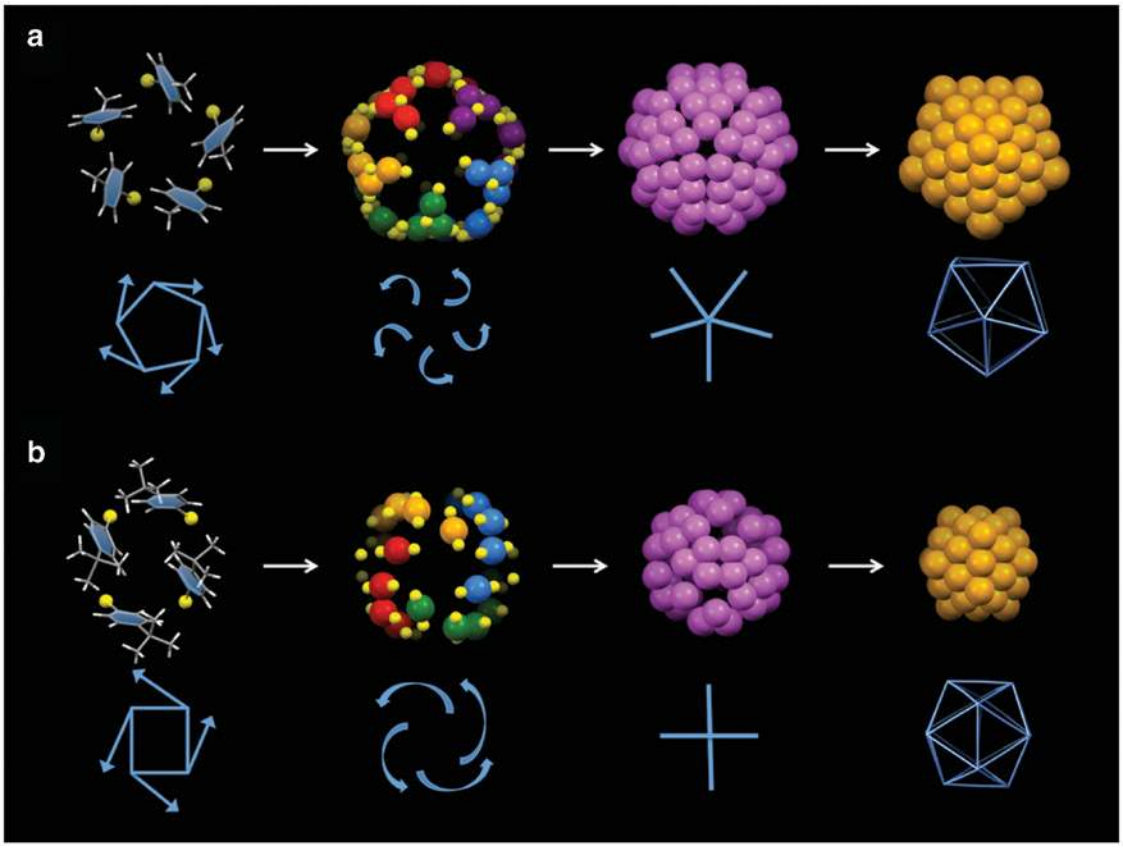


**Fig. 11:** The emergence of structural complexity in gold nanoparticles. (a) The five-fold rotative packing of *p*-MBT lead to a five-fold twinned decahedral kernel in $Au_{246}$(*p*-MBT)$_{80}$. (b) The four-fold rotative packing of *p*-TBBT leads to a 20-fold twinned icosahedral kernel in $Au_{133}$(*p*-TBBT)$_{52}$.

## Conclusions

In this focused review, we demonstrate that how the precision at the nanoscale can advance our understanding of nanomaterials and many critical issues in nanoscience. We first discuss the observation of a precise nanoscale transformation process induced by surface ligand exchange. Then we reveal the diversity of the gold nanocluster structures in both phases and surfaces. Among the diverse nanoclusters, we also find a periodic series of nanoclusters which have a uniform evolution of composition, structure and optical properties. Finally, we examine the nanocluster system from a perspective of molecular biology and uncover the intriguing emergence phenomena in the nanoparticle system. The precision at the nanoscale has great promises and would be an essential key to evolve current nanochemistry and nanoscience into a new era of innovation.

**Acknowledgements:** I am grateful to be selected as a recipient of the 2017 IUPAC-Solvay Prize for Young Chemists and to share my thesis work in the Pure & Applied Chemistry. I would also like to thank Prof. Rongchao Jin for editing this work as well as his support, guidance, and inspirations during my PhD study and future career. C.Z. is currently a NatureNet Postdoctoral Fellow with Prof. Christopher Murray and Prof. Cherie Kagan at Upenn.

## References

[1] M. C. Scott, C.-C. Chen, M. Mecklenburg, C. Zhu, R. Xu, P. Ercius, U. Dahmen, B. C. Regan, J. Miao. *Nature* **483**, 444 (2012).

[2] M. Haider, S. Uhlemann, E. Schwan, H. Rose, B. Kabius, K. Urban. *Nature* **392**, 768 (1998).
[3] Z. Y. Li, N. P. Young, M. Di Vece, S. Palomba, R. E. Palmer, A. L. Bleloch, B. C. Curley, R. L. Johnston, J. Jiang, J. Yuan. *Nature* **451**, 46 (2008).
[4] S. Van Aert, K. J. Batenburg, M. D. Rossell, R. Erni, G. Van Tendeloo. *Nature* **470**, 374 (2011).
[5] M. Azubel, J. Koivisto, S. Malola, D. Bushnell, G. L. Hura, A. L. Koh, H. Tsunoyama, T. Tsukuda, M. Pettersson, H. Häkkinen, R. D. Kornberg. *Science* **345**, 909 (2014).
[6] H. Zheng, R. K. Smith, Y. W. Jun, C. Kisielowski, U. Dahmen, A. P. Alivisatos. *Science* **324**, 1309 (2009).
[7] J. Park, H. Elmlund, P. Ercius, J. M. Yuk, D. T. Limmer, Q. Chen, K. Kim, S. H. Han, D. A. Weitz, A. Zettl, A. P. Alivisatos. *Science* **349**, 290 (2015).
[8] X. Ye, M. R. Jones, L. B. Frechette, Q. Chen, A. S. Powers, P. Ercius, G. Dunn, G. M. Rotskoff, S. C. Nguyen, V. P. Adiga, A. Zettl, E. Rabani, P. L. Geissler, A. P. Alivisatos. *Science* **354**, 874 (2016).
[9] C. Zeng, R. Jin. Gold nanoclusters: size-controlled synthesis and crystal structures, in *Gold Clusters, Colloids and Nanoparticles I. Structure and Bonding*, D. Mingos (Ed.), vol. 161, pp. 87–115, Springer, Cham (2014).
10] H. Qian, M. Zhu, Z. Wu, R. Jin. *Acc. Chem. Res.* **45**, 1470 (2012).
[11] R. Jin. *Nanoscale* **2**, 343 (2010).
[12] C. D. Bain, E. B. Troughton, Y. T. Tao, J. Evall, G. M. Whitesides, R. G. Nuzzo. *J. Am. Chem. Soc.* **111**, 321 (1989).
[13] R. G. Nuzzo, D. L. Allara. *J. Am. Chem. Soc.* **105**, 4481 (1983).
[14] M. Brust, M. Walker, D. Bethell, D. J. Schiffrin, R. Whyman. *J. Chem. Soc. Chem. Commun.* 801 (1994).
[15] M. Brust, J. Fink, D. Bethell, D. J. Schiffrin, C. Kiely. *J. Chem. Soc. Chem. Commun.* 1655 (1995).
[16] R. L. Whetten, J. T. Khoury, M. M. Alvarez, S. Murthy, I. Vezmar, Z. L. Wang, P. W. Stephens, C. L. Cleveland, W. D. Luedtke, U. Landman. *Adv. Mater.* **8**, 428 (1996).
[17] T. G. Schaaff, M. N. Shafigullin, J. T. Khoury, I. Vezmar, R. L. Whetten, W. G. Cullen, P. N. First, C. Gutierrez-Wing, J. Ascensio, M. J. Jose-Yacaman. *J. Phys. Chem. B* **101**, 7885 (1997).
[18] M. M. Alvarez, J. T. Khoury, T. G. Schaaff, M. Shafigullin, I. Vezmar, R. L. Whetten. *Chem. Phys. Lett.* **266**, 91 (1997).
[19] T. G. Schaaff, R. L. Whetten. *J. Phys. Chem. B* **103**, 9394 (1999).
[20] M. J. Hostetler, J. E. Wingate, C.-J. Zhong, J. E. Harris, R. W. Vachet, M. R. Clark, J. D. Londono, S. J. Green, J. J. Stokes, G. D. Wignall, G. L. Glish, M. D. Porter, N. D. Evans, R. W. Murray. *Langmuir* **14**, 17 (1998).
[21] V. L. Jimenez, M. C. Leopold, C. Mazzitelli, J. W. Jorgenson, R. W. Murray. *Anal. Chem.* **75**, 199 (2003).
[22] Y. Negishi, Y. Takasugi, S. Sato, H. Yao, K. Kimura, T. Tsukuda. *J. Am. Chem. Soc.* **126**, 6518 (2004).
[23] Y. Negishi, K. Nobusada, T. Tsukuda. *J. Am. Chem. Soc.* **127**, 5261 (2005).
[24] R. Jin, H. Qian, Z. Wu, Y. Zhu, M. Zhu, A. Mohanty, N. Garg. *J. Phys. Chem. Lett.* **1**, 2903 (2010).
[25] M. Zhu, E. Lanni, N. Garg, M. E. Bier, R. Jin. *J. Am. Chem. Soc.* **130**, 1138 (2008).
[26] Z. Wu, J. Suhan, R. Jin. *J. Mater. Chem.* **19**, 622 (2009).
[27] H. Qian, Y. Zhu, R. Jin. *ACS Nano* **3**, 3795 (2009).
[28] H. Qian, R. Jin. *Nano Lett.* **9**, 4083 (2009).
[29] H. Qian, R. Jin. *Chem. Mater.* **23**, 2209 (2011).
[30] C. Zeng, Y. Chen, A. Das, R. Jin. *J. Phys. Chem. Lett.* **6**, 2976 (2015).
[31] C. Zeng, H. Qian, T. Li, G. Li, N. L. Rosi, B. Yoon, R. N. Barnett, R. L. Whetten, U. Landman, R. Jin. *Angew. Chem. Int. Ed.* **51**, 13114 (2012).
[32] C. Zeng, T. Li, A. Das, N. L. Rosi, R. Jin. *J. Am. Chem. Soc.* **135**, 10011 (2013).
[33] C. Zeng, Y. Chen, K. Kirschbaum, K. Appavoo, M. Y. Sfeir, R. Jin. *Sci. Adv.* **1**, e1500045 (2015).
[34] Y. Chen, C. Zeng, D. R. Kauffman, R. Jin. *Nano Lett.* **15**, 3603 (2015).
[35] Y. Chen, C. Zeng, C. Liu, K. Kirschbaum, C. Gayathri, R. R. Gil, N. L. Rosi, R. Jin. *J. Am. Chem. Soc.* **137**, 10076 (2015).
[36] C. Zeng, C. Liu, Y. Pei, R. Jin. *ACS Nano* **7**, 6138 (2013).
[37] Z. Fan, X. Huang, Y. Han, M. Bosman, Q. Wang, Y. Zhu, Q. Liu, B. Li, Z. Zeng, J. Wu, W. Shi, S. Li, C. L. Gan, H. Zhang. *Nat. Commun.* **6**, 6571 (2015).
[38] H. Zhang, B. Gilbert, F. Huang, J. F. Banfield. *Nature* **424**, 1025 (2003).
[39] Q. Li, S. Wang, K. Kirschbaum, K. J. Lambright, A. Das, R. Jin. *Chem. Commun.* **52**, 5194 (2016).
[40] T. Higaki, C. Liu, Y. Chen, S. Zhao, C. Zeng, R. Jin, S. Wang, N. L. Rosi, R. Jin. *J. Phys. Chem. Lett.* **8**, 866 (2017).
[41] S. Ino. *J. Phys. Soc. Jap.* **27**, 941 (1969).
[42] L. D. Marks. *Rep. Prog. Phys.* **57**, 603 (1994).
[43] Z. L. Wang. *J. Phys. Chem. B* **104**, 1153 (2000).
[44] Y. Xia, Y. Xiong, B. Lim, S. E. Skrabalak. *Angew. Chem. Int. Ed.* **48**, 60 (2009).
[45] M. R. Langille, J. Zhang, M. L. Personick, S. Li, C. A. Mirkin. *Science* **337**, 954 (2012).
[46] C. L. Cleveland, U. Landman. *J. Chem. Phys.* **94**, 7376 (1991).
[47] F. Baletto, R. Ferrando. *Rev. Mod. Phys.* **77**, 371 (2005).
[48] M. Zhu, C. M. Aikens, F. J. Hollander, G. C. Schatz, R. Jin. *J. Am. Chem. Soc.* **130**, 5883 (2008).
[49] M. W. Heaven, A. Dass, P. S. White, K. M. Holt, R. W. Murray. *J. Am. Chem. Soc.* **130**, 3754 (2008).
[50] H. Qian, W. T. Eckenhoff, Y. Zhu, T. Pintauer, R. Jin. *J. Am. Chem. Soc.* **132**, 8280 (2010).

[51] P. D. Jadzinsky, G. Calero, C. J. Ackerson, D. A. Bushnell, R. D. Kornberg. *Science* **318**, 430 (2007).
[52] R. Jin, C. Zeng, M. Zhou, Y. Chen. *Chem. Rev.* **116**, 10346 (2016).
[53] C. Liu, T. Li, G. Li, K. Nobusada, C. Zeng, G. Pang, N. L. Rosi, R. Jin. *Angew. Chemie – Int. Ed.* **54**, 9826 (2015).
[54] T. Higaki, C. Liu, C. Zeng, R. Jin, Y. Chen, N. L. Rosi, R. Jin. *Angew. Chem. Int. Ed.* **55**, 6694 (2016).
[55] C. Zeng, C. Liu, Y. Chen, N. L. Rosi, R. Jin. *J. Am. Chem. Soc.* **138**, 8710 (2016).
[56] A. Mackay. *Acta Cryst.* **15**, 916 (1962).
[57] C. Zeng, Y. Chen, K. Kirschbaum, K. J. Lambright, R. Jin. *Science* **354**, 1580 (2016).
[58] J. C. Love, L. A. Estroff, J. K. Kriebel, R. G. Nuzzo, G. M. Whitesides. *Chem. Rev.* **105**, 1103 (2005).
[59] R. L. Whetten, R. C. Price. *Science* **318**, 407 (2007).
[60] H. Häkkinen. *Nat. Chem.* **4**, 443 (2012).
[61] O. Voznyy, J. J. Dubowski, J. T. Yates, P. Maksymovych. *J. Am. Chem. Soc.* **131**, 12989 (2009).
[62] P. Maksymovych, J. T. Yates. *J. Am. Chem. Soc.* **130**, 7518 (2008).
[63] D. E. Jiang. *Chem. Eur. J.* **17**, 12289 (2011).
[64] Y. Pei, Y. Gao, N. Shao, X. C. Zeng. *J. Am. Chem. Soc.* **131**, 13619 (2009).
[65] Y. Pei, R. Pal, C. Liu, Y. Gao, Z. Zhang, X. C. Zeng. *J. Am. Chem. Soc.* **134**, 3015 (2012).
[66] D. Jiang, W. Chen, R. L. Whetten, Z. Chen. *J. Phys. Chem. C* **113**, 16983 (2009).
[67] A. Das, T. Li, K. Nobusada, C. Zeng, N. L. Rosi, R. Jin. *J. Am. Chem. Soc.* **135**, 18264 (2013).
[68] A. Das, T. Li, G. Li, K. Nobusada, C. Zeng, N. L. Rosi, R. Jin. *Nanoscale* **6**, 6458 (2014).
[69] Y. Song, S. Wang, J. Zhang, X. Kang, S. Chen, P. Li, H. Sheng, M. Zhu. *J. Am. Chem. Soc.* **136**, 2963 (2014).
[70] C. Zeng, C. Liu, Y. Chen, N. L. Rosi, R. Jin. *J. Am. Chem. Soc.* **136**, 11922 (2014).
[71] Y. Pei, X. C. Zeng. *Nanoscale* **4**, 4054 (2012).
[72] R. Jin. *Nanoscale* **7**, 1549 (2015).
[73] C. Zeng, Y. Chen, K. Iida, K. Nobusada, K. Kirschbaum, K. J. Lambright, R. Jin. *J. Am. Chem. Soc.* **138**, 3950 (2016).
[74] C. Zeng, Y. Chen, G. Li, R. Jin. *Chem. Commun.* **50**, 55 (2014).
[75] C. Zeng, Y. Chen, C. Liu, K. Nobusada, N. L. Rosi, R. Jin. *Sci. Adv.* **1**, e1500425 (2015).
[76] P. Atkins, J. D. Paula. *Atkins' Physical Chemistry*, 8th ed., pp. 243–319, W. H. Freeman and Company, New York (2006).
[77] Cb. B. Murray, D. J. Norris, M. G. Bawendi, D. J. Noms, M. G. Bawendi. *J. Am. Chem. Soc.* **115**, 8706 (1993).
[78] W. W. Xu, Y. Li, Y. Gao, X. C. Zeng. *Nanoscale* **8**, 7396 (2016).
[79] Z. Ma, P. Wang, G. Zhou, J. Tang, H. Li, Y. Pei. *J. Phys. Chem. C* **120**, 13739 (2016).
[80] C. A. Hunter, J. K. M. Sanders. *J. Am. Chem. Soc.* **112**, 5525 (1990).
[81] M. Nishio. *Phys. Chem. Chem. Phys.* **13**, 13873 (2011).
[82] P. W. Anderson. *Science* **177**, 393 (1972).
[83] Q.-F. Sun, J. Iwasa, D. Ogawa, Y. Ishido, S. Sato, T. Ozeki, Y. Sei, K. Yamaguchi, M. Fujita. *Science* **328**, 1144 (2010).